HHS Public Access

Author manuscript

Proc SPIE Int Soc Opt Eng. Author manuscript; available in PMC 2023 June 22.

Published in final edited form as:

Proc SPIE Int Soc Opt Eng. 2019 February ; 10931: . doi:10.1117/12.2514579.

MEMS-in-the-lens 3D beam scanner for *in vivo* microscopy

David L. Dickensheets[*,a], **Tianbo Liu**[a], **Milind Rajadhyaksha**[b]

[a]Electrical and Computer Engineering Department, Montana State University, Bozeman, MT 59715, USA

[b]Dermatology Department, Memorial Sloan Kettering Cancer Center, New York, New York 10022, USA.

Abstract

The “MEMS-in-the-lens” active lens for a laser scanning microscope comprises a high numerical aperture front element, a 3D+ MOEMS beam scanner and a collimating back lens. The scanner utilizes a silicon gimbal with SU-8 polymer flexures and deformable membrane mirror. The mirror aperture is 4 mm in diameter, and is capable of 9 μm deflection for focus control, with four annular electrodes to allow tuning of primary and secondary spherical aberration. The gimbal supports tip/tilt actuation up to ±3° for lateral beam scanning. We show confocal imaging using a benchtop mockup of the active lens, illustrating the potential for this approach to support 3D microscopy for optical biopsy applications.

Keywords

MEMS Scan Mirror; MOEMS 3D Scanner; Active Optics; Variable Focus Mirror; Variable Focus Lens

1. INTRODUCTION

High-resolution scanning laser microscopy techniques, such as confocal laser scanning microscopy (CLSM) and two-photon microscopy (TPM), rely on high numerical aperture (N.A.) optics to image hundreds of micrometers beneath the surface of living tissue, providing a picture of tissue structure, cellular organization and details such as nuclear size. Many applications in healthcare, developmental biology and neuroscience will benefit from miniaturization of the optical microscope, to make it suitable as a handheld, endoscopic or animal-wearable instrument. Toward this goal, micro-mirror scanners have been developed to replace bulky galvanometer scanners, often combining two-dimensional scanning into a single mirror. There has also been progress to provide focus control in a miniaturized instrument using variable focus lenses[1,2] or mirrors,[3,4,5] piston mirrors,[6,7] or lens scanners.[8,9]

The need to maintain a large N.A. in the tissue increases the complexity of the optical system. Because the working distance of the objective lens is very short, the scanner cannot

[*]Corresponding Author: davidd@montana.edu; phone: +1 406 994-7874.

be placed between the lens and the tissue; therefore, optics after the scanner (between the scanner and the tissue) must be aberration-corrected over a finite field-of-view (FOV). A typical implementation deploys the MEMS scan mirror in a space where the beam is collimated, located at or imaged onto the back focal plane of a well-corrected objective lens (MEMS-before-the-lens architecture). In this case, the miniature instrument mimics the traditional benchtop scanning laser microscope. There has been progress to develop miniaturized lenses that can meet the high N.A. requirements of CLSM and TPM, and to demonstrate compact MEMS-scanned instruments.[10,11,12] However, the need to fully correct for off-axis aberrations at high N.A. leads to multiple glass elements and long optical paths, making miniaturization difficult.

Recently we have begun to explore an alternative architecture that places the MEMS scanner within the objective lens, between a low N.A. “back lens” and an aplanatic “front lens” to increase the N.A. of the beam in the tissue.[13,14,15] We call this the MEMS-in-the-lens architecture. The back lens only needs to be corrected on-axis; a single aspheric lens can serve as the back lens for monochromatic imaging. The front lens should be aplanatic (corrected for spherical aberration and coma); if it is also anastigmatic (corrected for spherical aberration, coma and astigmatism) then it can support imaging over an even wider field of view. The MEMS-in-the-lens architecture therefore can provide well-corrected imaging over a usefully large lateral (2D) field of view in the tissue, at a particular depth where the correction is optimized. If the scanner can adjust spherical aberration in concert with a focus adjustment, then the well-corrected field of view can be increased to include a 3D volume of tissue, as required by most imaging applications. In this paper we describe such a system, in which the MEMS 3D+ scanner is the tip/tilt/curvature type, with the ability to tune primary and secondary spherical aberration so as to maximize the well-corrected 3D field of view.

2. HEMISPHERE AND HYPERHEMISPHERE WITH ACTIVE OPTICAL SCANNER

2.1 Aplanatic hemisphere front lens (solid immersion lens)

There are two aplanatic solutions for a spherical glass lens, for which imaging is devoid of all spherical aberration and circular coma. One pair of aplanatic points is at the center of curvature of the glass surface, resulting in a hemisphere lens, also called a solid immersion lens when used in contact with the surface to be imaged. The hemisphere lens increases the NA of the beam by the index of refraction n_g of the glass. Despite being aplanatic, the hemisphere lens suffers from astigmatism which will limit the lateral field of view for sufficiently large scan angles.

2.2 Anastigmatic hyperhemisphere front lens

The second pair of aplanatic points are found on the optical axis, the first at a distance $R(1 + 1 / n_g)$ from the apex of the lens inside the glass, and the second at a distance $R(1 + n_g)$ from the apex of the lens in air (a virtual focus). A hyperhemisphere glass lens with index of refraction n_g with radius of curvature R and thickness $R(1 + 1 / n_g)$, when used in contact with the surface to be imaged, forms an aplanatic virtual image of that surface. In

the case of the hyperhemisphere lens, the NA of the beam in air is increased by n_g^2 after refraction at the lens surface. In addition to being aplanatic, the hyperhemisphere lens is also anastigmatic, being devoid of astigmatism as well as coma and spherical aberration. Therefore, the hyperhemisphere lens provides a much larger diffraction-limited field of view, compared to the hemisphere lens. A truncated hyperhemisphere lens remains nearly anastigmatic, but allows the depth of best correction to be located beneath the surface of the tissue.

2.3 Simulated performance with an active scanner to provide 3D beam scanning

We propose to locate a beam scanner adjacent to the hemisphere or hyperhemisphere lens. The scanner should be able to move the focus of the beam in x, y, and z. To better understand the potential performance and the limits of this configuration, we performed preliminary raytrace analysis in Zemax, computing Strehl ratio S as a metric to determine the size of the 3D volume of tissue that could be imaged with good fidelity. We interpret $S > 0.8$ as being "diffraction limited." We assume that the scanner will serve as the aperture stop of the system.

The results of this simulation are summarized in Figure 1. We compared a 2 mm radius hemisphere lens to a 2 mm radius hyperhemisphere lens, maintaining N.A.=0.7 in the tissue for both lenses. The aperture stop (which will be the location for the beam scanner) is 2.5 mm before the lens. We evaluated the performance within a cylinder of tissue 450 μm in diameter and 200 μm thick, in contact with the lens. Figure 1(a) depicts the hemisphere simulation, and Figure 1(d) depicts the hyperhemisphere simulation. For the hemisphere with this stop position, the field of view represents a maximum beam angle of approximately ±4.3°. For the hyperhemisphere and this stop position, the field of view represents a maximum beam angle of ±4°.

Figure 1(b) depicts the Strehl map for the hemisphere lens. Just beneath the surface of the lens, performance is diffraction limited to a lateral field of view of approximately 140 μm. For greater beam angles, astigmatism is the dominant aberration that limits the performance. At deeper focus positions, spherical aberration and coma begin to increase, limiting even the on-axis performance. Beyond a depth of approximately 190 μm performance ceases to be diffraction limited. For the full 450 μm x 200 μm cylinder, the average Strehl is 0.17, with diffraction limited performance achieved over 6.4% of the volume.

Figure 1(e) depicts the Strehl map for the truncated hyperhemisphere lens. At a depth of 100 μm beneath the surface of the lens, performance is diffraction limited to a lateral field of view of more than 450 μm. At shallower and deeper focus positions, spherical aberration and coma begin to increase, limiting performance. Beyond a depth of approximately 125 μm, performance ceases to be diffraction limited. For the full 450 μm x 200 μm cylinder, the average Strehl is 0.56, with diffraction limited performance achieved over 29% of the volume.

If, in addition to $x - y - z$ scanning, the scanner can adjust spherical aberration with depth, then the volume over which diffraction limited performance is possible can be increased. Figure 1(c) depicts the Strehl map for the hemisphere lens, but now with the scanner

compensating primary and secondary spherical aberration as the focal depth is varied. Notice that on-axis performance is restored throughout the depth of the tissue. But the dominant off-axis aberration of astigmatism is unaffected, and the lateral field of view remains limited at about 140 μm. Average Strehl has increased to .18, and the diffraction limited volume percent has increased to 9.5%.

Figure 1(f) depicts the Strehl map for the hyperhemisphere lens with spherical aberration correction. Again, on-axis the performance is restored throughout the full 200 μm depth. The diffraction-limited lateral field of view exceeds 150 μm throughout the full 200 μm depth, with a zone about 60 μm thick that is diffraction limited over a field of view in excess of 450 μm. Off-axis performance above and below this zone is limited by a mixture of coma and astigmatism. The average Strehl here is 0.76 over the full 450 μm x 200 μm cylinder, with diffraction-limited performance achieved over 58% of that volume.

3. MEMS-IN-THE-LENS SYSTEM ARCHITECTURE

3.1 Compact system with folded annular beam

Based on encouraging results from the raytrace analysis, we chose to investigate an optical architecture that places a 3D+ MOEMS scanner within a lens, using a hyperhemisphere front lens to achieve N.A. of 0.7 in the tissue. The MOEMS scanner is a gimbal-mounted mirror with a deformable surface, to control x and y beam tilt and z position of focus. Concentric annular electrodes on the mirror allow for shaping the deflection force radially, to control asphericity of the surface. Because this is a mirror, we must provide a fold in the beam path, using either a beam splitter or a mirror. The aberrations of a focus-control deformable mirror increase as the incidence angle of the chief ray increases.[16] We elected to keep the chief ray at normal incidence. To avoid a beam splitter, with its attendant optical losses and polarization dependencies, we adopted a folded annular beam for our lens. The system concept is illustrated in Figure 2. The MOEMS scanner is provided with an open annular aperture around its circumference to allow the forward beam to pass. A retro-reflecting ring directs the converging beam back onto the mirror, which then redirects the beam onto the hyperhemisphere lens. The central obscuration extends to approximately 70% of the pupil diameter.

3.2 Comparing tip/tilt/piston mirror to tip/tilt/curvature mirror for high N.A. performance

With the architecture depicted on Figure 2, the mirror reflects a converging optical beam. Rotation of the mirror about the x and y axes effects lateral scanning of the focus position (tip/tilt actuation). Scanning in z can be achieved with either piston motion of the mirror or tuning of the mirror curvature. We compare the requirements placed on the MOEMS mirror to achieve $\Delta z = 100\,\mu\text{m}$ scanning axially, for these two types of scan mirrors, benchmarking them for N.A.=0.7 and assuming a hyperhemisphere lens.

For a piston mirror, translation of the mirror surface by d moves the virtual focus z_1 of a reflected, converging beam a distance $2d$ axially. For small deflections, the axial magnification scales as the ratio of N.A. squared, so that $(z_1 / n_1) / (z_2 / n_2) = ((NA_2) / (NA_1))^2$. In our case, $n_1 = 1.0$ in air, while $n_2 = n_s$ is the index of refraction of the tissue. The

hyperhemisphere magnifies the N.A. by n_g^2, where n_g is the index of refraction of the glass. Therefore, the mirror displacement may be computed using

$$d = \Delta z\left(\frac{n_g^4}{2n_s}\right).$$

Assuming $n_g = 1.5$ and $n_s = 1.34$, $\Delta z = 100\,\mu\text{m}$ focus displacement requires $d = 189\,\mu\text{m}$ piston motion, independent of the N.A. in the tissue.

For a variable curvature mirror, the mirror sag δ depends on defocus and N.A. according to[17]

$$\delta = \Delta z\frac{NA^2}{4n_s}.$$

Again, with $n_s = 1.34$ and N.A. = 0.7, $\Delta z = 100\,\mu\text{m}$ focus displacement demands a mirror sag of $\delta = 9.1\,\mu\text{m}$. For large defocus range, even at moderately high N.A., the mechanical displacement demanded of a curvature control mirror is much less than the displacement needed from a piston mirror, allowing the use of stiffer and therefore faster actuators to achieve focus control. An important additional benefit of a deformable mirror surface is the direct extension of electronic control over asphericity of the surface, without a major change to the scanner construction.

4. MOEMS 3D+ BEAM SCANNER FOR MEMS-IN-THE-LENS SYSTEM

4.1 $X - Y$ gimbal mirror with deformable membrane surface

A 3D+ MOEMS tip/tilt/curvature mirror was first introduced by Shao in 2004.[18] That mirror utilized low stress silicon rich LPCVD silicon nitride as a deformable membrane material, with the membrane suspended on a rigid plate, the plate itself gimbal-mounted for 2D lateral beam scanning. The mirror was 700 μm in diameter, and achieved 3 μm center deflection for defocus as the z-scan mechanism. Two concentric electrodes allowed for some tuning of primary spherical aberration. The mirror we have developed for the MEMS-in-the-lens scanner, which is depicted in Figure 3, offers several improvements over Shao's device. The mirror surface is 4 mn in diameter, as required for our initial optical designs. The membrane material is the polymer SU-8, which can have tensile stress an order of magnitude lower than the low-stress LPCVD silicon nitride film. This allows greater deformation of the membrane, utilizing a larger air gap, while maintaining reasonable defocus control voltages. The mirror has demonstrated 9 μm variable surface sag, providing approximately 3 times greater focus control range in the sample. Four concentric electrodes provide more degrees of freedom for aberration control, and we have characterized independent control over both primary and secondary spherical aberration. SU-8 is also used for the torsional flexures, and the mirror has demonstrated up to ±3° mechanical rotation for the inner (resonant) axis, giving a θD product of 12 deg-mm, compared to 2.8 deg-mm for Shao's mirror. Complete details about the mirror fabrication and characterization have been previously provided.[15]

For beam scanning, the 3D+ mirror provides raster scanning with a resonant sinusoidal scan on the inner axis, near a frequency of 1 kHz, and a non-resonant sawtooth scan on the outer axis at a user specified frequency. When operated in a quasi-static (non-resonant) mode, the outer axis achieves ±1.7° mechanical rotation. The deformable mirror can provide more than 9 μm surface sag for defocus (18 μm wavefront sag for the reflected beam, equivalent to a normalized Zernike defocus coefficient $a_{2,0} = 5.2\,\mu m$). With a bias deflection of 3.7 μm at the membrane center (wavefront $a_{2,0} = 2.1\,\mu m$), the mirror can correct primary spherical aberration of the wavefront over a range of $a_{4,0} = -132\,nm$ to +228 nm, and secondary spherical over a range of $a_{6,0} = -178\,nm$ to +132 nm. All Zernike coefficients are normalized so that the coefficient is equivalent to the rms wavefront deflection for that mode.

5. BENCHTOP DEMONSTRATION MEMS-IN-THE-LENS SYSTEM FOR CONFOCAL MICROSCOPY

We constructed a benchtop confocal microscope to demonstrate imaging using the MEMS-in-the-lens architecture and our prototype scan mirror. The system is illustrated in Figure 4. Light from a helium-neon laser at 633 nm is spatially filtered by coupling through a single mode fiber. A compound lens serves as the back lens for the system, generating a diffraction-limited, converging beam, incident on the MOEMS scanner. The hyperhemisphere lens is constructed using a 2 mm diameter half-ball lens cemented to a 500 μm thick glass plate. The sample is placed in contact with the glass, using ultrasound gel as an index matching medium. The obscuration formed by the sample and the hyperhemisphere lens results in an annular pupil for the system. Backscattered light is focused onto the pinhole, and detected by an avalanche photodiode.

The effective N.A. in the sample is 0.57. The N.A. at the pinhole is 0.06, and the pinhole diameter is 10 μm. Figure 5 shows the measured edge response (0.55 μm 20%-80% edge width) and axial response when imaging a plane mirror (6.1 μm FWHM). The index of refraction of the medium adjacent to the edge and mirror for these measurements is $n_s = 1.51$. The axial focus range we could address in an aqueous sample ($n_s = 1.34$) was approximately $\Delta z = 125\,\mu m$, with 150V applied to all zones of the focus control membrane, which corresponded to a mirror sag of approximately $\delta = 7.5\,\mu m$.

We imaged a portion of a detached membrane from a failed device (Figure 6a), adhered to the sample stage with index matching gel. The vias in the image are 5 μm wide, arranged in a square grid with 30 μm grid spacing. Some lateral distortion is present in the image, attributed to misalignment between the gimbal scanner and the quadrant electrodes underneath. The overall field of view is approximately 390 μm by 180 μm, corresponding to an angular scan of the mirror of ±1.6° mechanical in the fast axis (horizontal) and ±0.75° in the slow axis (vertical). Figure 6b is an image of cheek cells, with dilute acetic acid used to increase nuclear contrast. Cell membranes and nuclei are visible in the image.

6. SUMMARY

We have explored a concept for a compact MOEMS-scanned laser scanning microscope, proposing to use active beam scanning with dynamic correction of spherical aberration in

order to simplify the high N.A. optical lens. We found that a single hyperhemisphere, used at a moderately large N.A. of 0.7, provides a wide diffraction-limited field of view, but only at a specific depth in the sample where aberrations are minimized. We showed simulations predicting that, with tunable spherical aberration at the MOEMS scanner, this well-corrected field of view can be extended throughout a 200 μm depth in tissue, approximately doubling the volume of tissue that can be imaged with diffraction-limited performance. We also showed preliminary imaging results using a newly developed MOEMS 3D+ scan mirror in a benchtop mockup of the MEMS-in-the-lens architecture. These early images indicate that the concept holds promise as an architecture that can deliver high fidelity laser scanning microscopy with a very compact opto-mechanical footprint.

ACKNOWLEDGEMENTS

This work was supported by the NIH through the National Institute of Biomedical Imaging and Bioengineering (NIBIB) (1R21EB018507) and the National Cancer Institute (NCI) (P30CA008748). The work was performed in part at the Montana Nanotechnology Facility and at the Cornell Nanoscience Facility, both members of the National Science Foundation NNCI program supported by NSF Grants ECCS-1542210 and ECCS-1542081.

REFERENCES

[1]. Aljasem Khaled, Werber Armin, Seifert Andreas, Zappe Hans, “Fiber optic tunable probe for endoscopic optical coherence tomography,” J. Opt. A: Pure Appl. Opt 10 044012, 2008.

[2]. Zeng Xuefeng and Jiang Hongrui, “Liquid tunable microlenses based on MEMS techniques,” J. Phys. D: Appl. Phys 46 323001, 2013. [PubMed: 24163480]

[3]. Yang Victor X. D., Mao Youxin, Standish Beau A., Munce Nigel R., Chiu Stephanie, Burnes Daina, Wilson Brian C., and Vitkin I. Alex, Himmer Phillip A. and Dickensheets David L., “Doppler optical coherence tomography with a micro-electro-mechanical membrane mirror for high-speed dynamic focus tracking,” Optics Letters, Vol. 31, No. 9, pp 1262–1264, May 2006. [PubMed: 16642079]

[4]. Moghimi Mohammad J., Wilson Chris and Dickensheets David L., “Improved MOEMS deformable mirror for in vivo optical microscopy,” J. Micro/Nanolithography, MEMS and MOEMS, 11(4), 043006 Oct 12, 2012.

[5]. Lukes Sarah J., Downey Ryan D., Kreitinger Seth T., and Dickensheets David L.. "Four-zone varifocus mirrors with adaptive control of primary and higher-order spherical aberration." Applied Optics 55, no. 19, 5208–5218, 2016. [PubMed: 27409212]

[6]. Li Haijun; Duan Xiyu; Li Gaoming; Oldham KennR.; Wang Thomas D., "An Electrostatic MEMS Translational Scanner with Large Out-of-Plane Stroke for Remote Axial-Scanning in Multi-Photon Microscopy." Micromachines 8, no. 5: 159, 2017.

[7]. Zhang X; Zhou L; Xie H A fast, large-stroke electrothermal MEMS mirror based on Cu/W bimorph. Micromachines, 6, 1876–1889, 2015.

[8]. Kwon S and Lee LP, "Micromachined transmissive scanning confocal microscope," Opt. Lett 29, 706–708 (2004). [PubMed: 15072365]

[9]. Park Hyeon-Cheol, Song Cheol, and Jeong Ki-Hun, “Micromachined lens microstages for two-dimensional forward optical scanning,” Opt. Express 18, 16133–16138 (2010). [PubMed: 20720998]

[10]. Duan Xiyu, Li Haijun, Qiu Zhen, Joshi Bishnu P., Pant Asha, Smith Arlene, Kurabayashi Katsuo, Oldham Kenn R., and Wang Thomas D., "MEMS-based multiphoton endomicroscope for repetitive imaging of mouse colon," Biomed. Opt. Express 6, 3074–3083 (2015). [PubMed: 26309768]

[11]. Liang Chen, Sung Kung-Bin, Richards-Kortum Rebecca R., and Descour Michael R., "Design of a high-numerical-aperture miniature microscope objective for an endoscopic fiber confocal reflectance microscope," Appl. Opt 41, 4603–4610 (2002). [PubMed: 12153093]

[12]. Kester Robert T., Tkaczyk Tomasz S., Descour Michael R., Christenson Todd, and Richards-Kortum Rebecca, "High numerical aperture microendoscope objective for a fiber confocal reflectance microscope," Opt. Express 15, 2409–2420 (2007). [PubMed: 19532478]

[13]. Liu Tianbo, and Dickensheets David L.. "3-dimensional beam scanner for a handheld confocal dermoscope." International Conference on Optical MEMS and Nanophotonics (OMN 2016), IEEE, 2016.

[14]. Dickensheets David L., Liu Tianbo, Kreitinger Seth, Peterson Gary, and Rajadhyaksha Milind, “Toward Smaller, More Useable Clinical Confocal Microscopes with Advanced Scanning and Integrated Wide-Field Guidance,” in Biophotonics Congress: Biomedical Optics Congress 2018 (Microscopy/ Translational/Brain/OTS), OSA Technical Digest (Optical Society of America, 2018), paper MW4A.1, 3–6 April, 2018.

[15]. Liu Tianbo, Svidunovich Aaron J., Wollant Benjamin C., and Dickensheets David L., "MEMS 3-D Scan Mirror With SU-8 Membrane and Flexures for High NA Microscopy," IEEE J. Microelectromechanical Systems, Vol. 27 No. 4, pp. 719–729, 2018.

[16]. Lukes Sarah, “Imaging performance of elliptical-boundary varifocal mirrors in active optical systems,” Ph.D. Dissertation, Montana State University, (https://scholarworks.montana.edu/xmlui/handle/1/8862), 2015.

[17]. Dickensheets David L., “Requirements of MEMS membrane mirrors for focus adjustment and aberration correction in endoscopic confocal and optical coherence tomography imaging instruments,” J. Micro/Nanolithography, MEMS and MOEMS Vol. 7, 021008, Apr. 30, 2008.

[18]. Shao Yuhe, Dickensheets DL and Himmer P, "3-D MOEMS mirror for laser beam pointing and focus control," IEEE Journal of Selected Topics in Quantum Electronics, vol. 10, no. 3, pp. 528–535, May-June 2004.

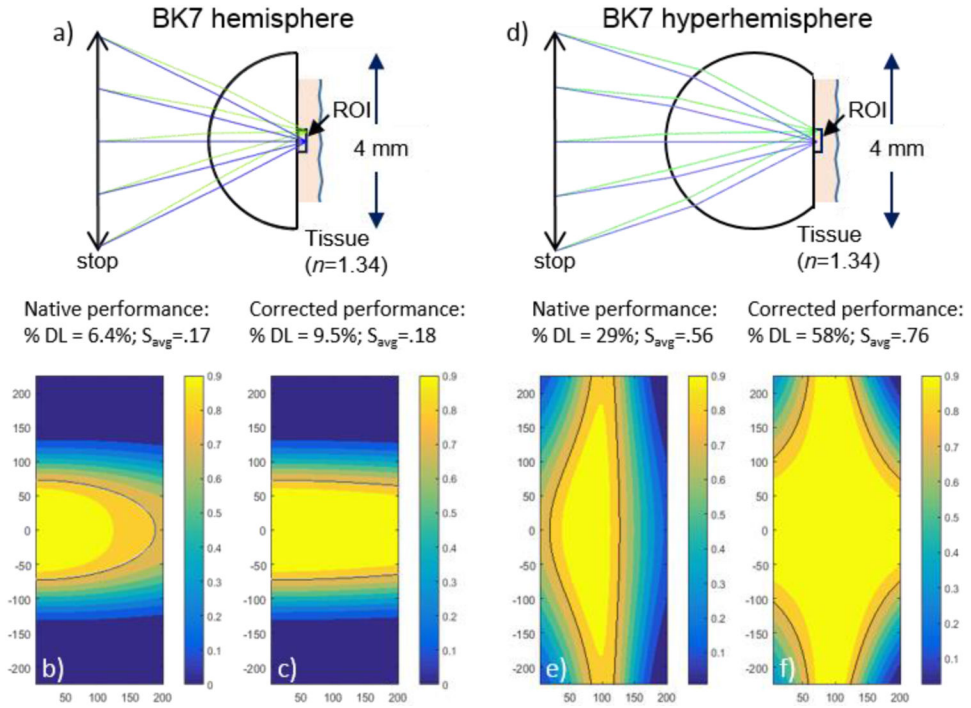

Figure 1.

Results of raytrace analysis to determine Strehl ratio throughout a 3D region of interest (ROI) in the tissue beneath the lens. (a) and (d) show the simulation configurations; (b), (c), (e) and (f) are contour plots of Strehl ratio over an axial cross section of a region of interest that is 450 μm in diameter laterally and 200 μm deep. The black line shows the $S = 0.8$ contour. The hemisphere lens shown in (a) is aplanatic at the glass-tissue interface (no coma or spherical aberration). b) With no correction of spherical aberration with depth, the performance falls off as the focal point is positioned deeper beneath the surface. c) With correction of spherical aberration with depth, the performance can be extended throughout the 200 μm thickness used for this simulation. For the hemisphere lens, the lateral field of view of both (b) and (c) is limited by uncorrected astigmatism. The hyperhemisphere lens shown in (d) is slightly thinner than $R(1 + 1 / n_g)$, causing the depth of best correction to occur at 100 μm into the tissue. e) With no active control over spherical aberration, the performance decays axially as well as laterally. f) With correction of spherical aberration with depth, performance on-axis can be extended throughout the 200 μm thickness used for this simulation. At the “natural” depth for the hyperhemisphere, the lens is approximately anastigmatic, with a very wide lateral field of view. Shallower and deeper, the aberrations grow with contribution from both coma and astigmatism contributing to reduced Strehl ratio.

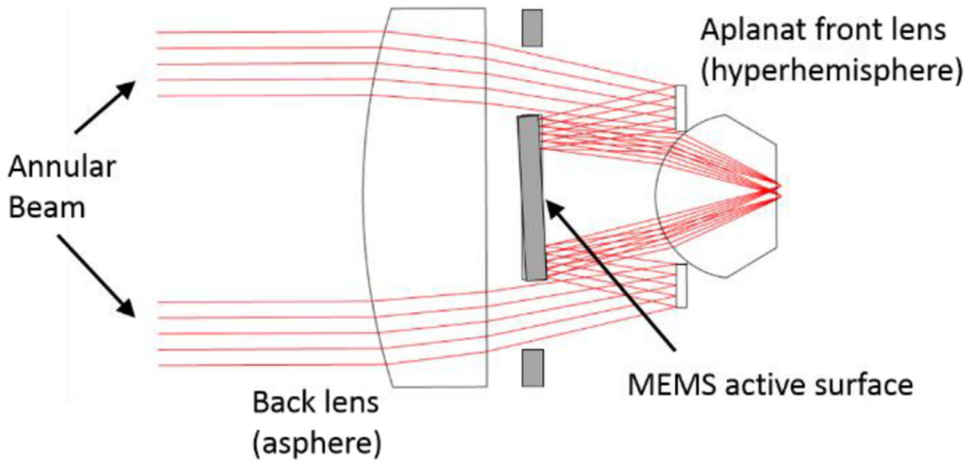

Figure 2.
MEMS-in-the-lens architecture with a folded annular beam and a tip/tilt/curvature MOEMS beam scanner.

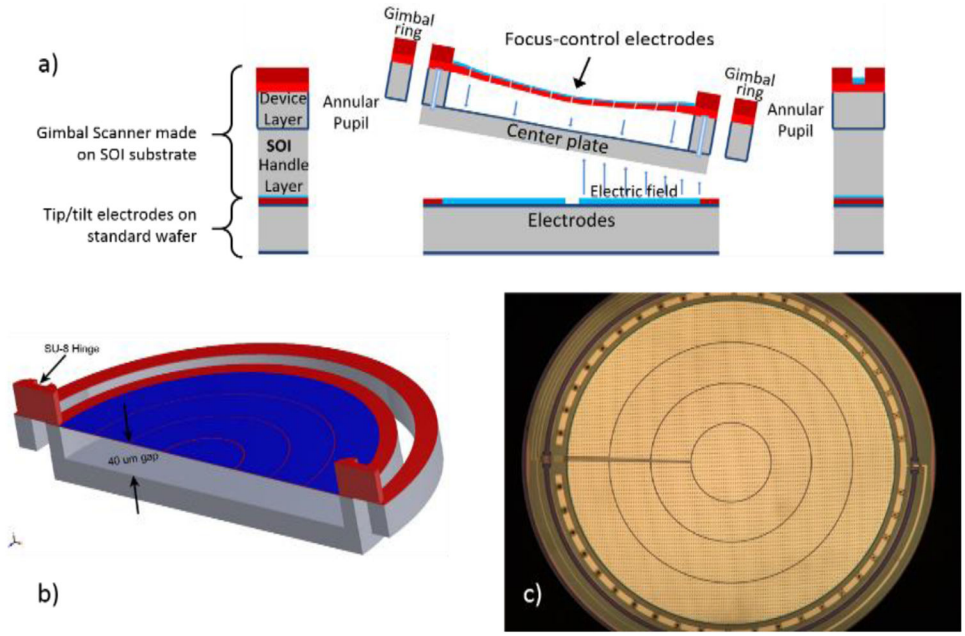

Figure 3.

3D+ MOEMS scanner, with deformable membrane mirror suspended from a gimbal-supported center plate. Membrane deflection is controlled by four concentric electrodes on the mirror surface. Tip/tilt scanning is controlled by quadrant electrodes underneath the center plate. a) Cross sectional view showing gimbal scanner made on an SOI wafer, bonded to a second wafer with patterned quadrant tip/tilt control electrodes; b) Solidworks model of the gimbal structure with thick SU-8 hinges and thin SU-8 membrane with patterned aluminum layer; c) Optical microscope image of the finished gimbal scanner, showing patterned reflective mirror surface with control electrodes.

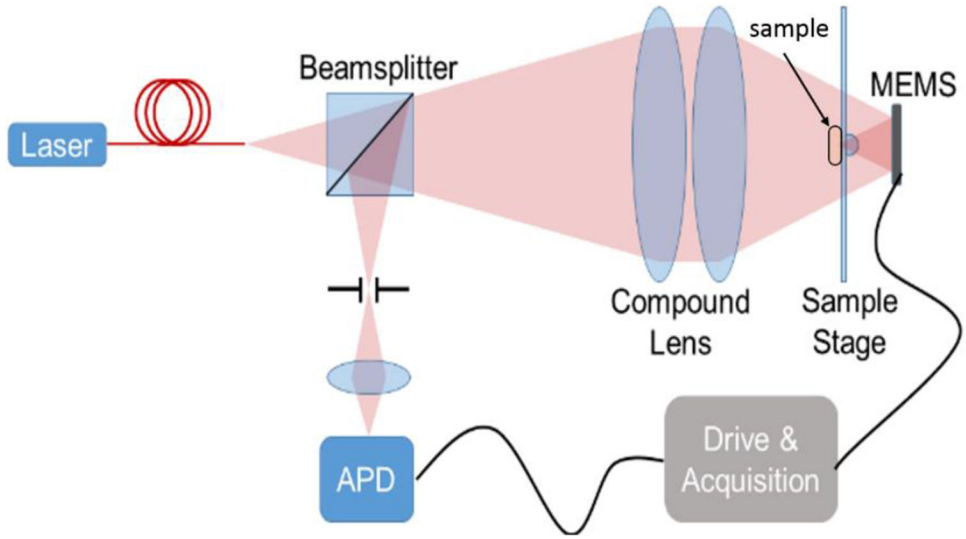

Figure 4.
Benchtop confocal microscope.

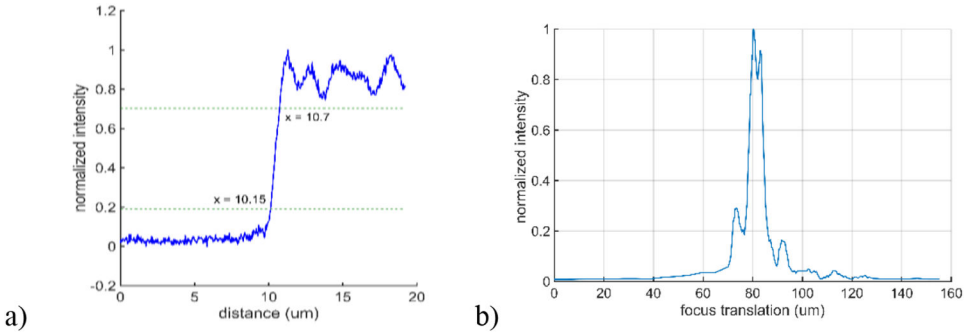

Figure 5.
Measured edge and axial response of the benchtop MEMS-in-the-lens confocal microscope.

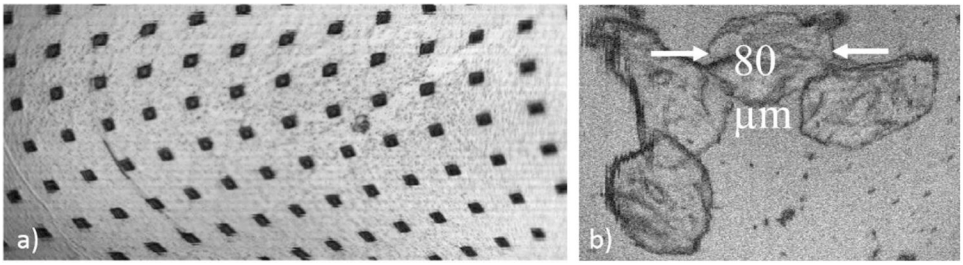

Figure 6.

a) Image of the surface of a portion of a broken MOEMS mirror. The via openings in the metal film are 5 μm wide, and on a 30 μm grid spacing. b) Image of cheek cells.